JMEPEG (2011) 20:597–604
DOI: 10.1007/s11665-011-9852-0

1059-9495/$19.00

Stress-Induced Martensite in Front of Crack Tips in NiTi Shape Memory Alloys: Modeling Versus Experiments

C. Maletta and M.L. Young

(Submitted June 7, 2010; in revised form December 30, 2010)

NiTi-based shape memory alloys (SMAs) exhibit an unusual stress distribution at the crack tip as compared to common engineering materials, due to a stress-induced martensitic transformation resulting from highly localized stresses. Understanding the fracture mechanics of NiTi-based SMAs is critical to many of their applications. Here, we develop an analytical model, which predicts the boundaries of the transformation region in the crack tip vicinity of NiTi-based SMAs. The proposed model is based on a recent analytical approach which uses modified linear elastic fracture mechanics concepts to predict the crack tip stress distribution and transformation region in SMAs but, unfortunately, it applies only to the plane stress condition. To overcome this limitation, the proposed model accounts for stress triaxiality, which plays an important role in restricting crack tip plastic deformations in common ductile metals as well as the stress-induced martensite in NiTi SMAs. The effects of triaxial stress at the crack tip are taken into account by including a new parameter, the transformation constraint factor, which is based on the plastic constraint factor of elasto-plastic materials. The predictions of the model are compared with synchrotron x-ray micro-diffraction observations and satisfactory agreement is observed between the two results. Finally, the evolution of crack tip transformation boundaries during fracture tests of miniature compact tension specimens is predicted and the effects of applied load and crack length are discussed.

Keywords fracture mechanics, nickel-titanium alloys, shape memory alloys, stress-induced transformation

1. Introduction

NiTi shape memory alloys (SMAs) have seen a growing interest in many engineering and medical applications due to their unique functional properties, specifically the shape memory effect (SME) and the superelastic effect (SE) (Ref 1), as well as to their good mechanical performance and biocompatibility. Due to the SME and SE, NiTi SMAs exhibit unique features such as the ability to recover large strains and/or to support large mechanical loads over a wide range of deformations, thanks to a reversible solid state phase transformation (thermoelastic martensitic transformation) that can be activated either by temperature (i.e., thermally-induced martensitic transformation), or by applied stress (i.e., stress-induced martensitic transformation) (Ref 1). As a consequence of the high scientific and technological interest of NiTi SMAs, extensive research has been carried out to better understand their thermo-mechanical properties (Ref 2), and several numerical models have been developed, which are able to predict both their mechanical and functional behaviors (Ref 3). Despite this scientific and technological interest, many aspects related to the mechanical properties of NiTi SMAs have not been thoroughly investigated, especially in the field of fracture mechanics and fatigue, which are strongly affected by thermoelastic martensitic transformation. In fact, from a material science point of view, significant differences with respect to common engineering metals are observed and, consequently, well-known theories on mechanics of materials fail to adequately describe fracture and fatigue phenomena in SMAs and, therefore, they must be modified to account for these phenomena. In particular, it is widely accepted that thermoelastic martensitic transformation, and specifically stress-induced martensitic transformation, plays a significant role in the fracture process of NiTi SMAs (Ref 4-12). Experimental studies have focused on understanding the formation and propagation of cracks under variable loadings (Ref 4, 5) as well as under static loading conditions (Ref 6-12). The formation of stress-induced martensite in the crack tip vicinity, as a consequence of the highly localized stresses, has been observed using digital image correlation (DIC) (Ref 6), by infrared (IR) thermography (Ref 10), and by synchrotron x-ray diffraction (XRD) (Ref 7-9). Furthermore, the IR thermography investigation, which illuminates heat effects associated with the stress-induced transformation, revealed the reversibility of the crack tip phase transformation during unloading (Ref 10).

Recently, finite element (FE) simulations have been carried out to better understand the effects of phase transformation on the crack tip stress distribution (Ref 13-16). These simulations use commercial FE software codes and standard elasto-plastic solutions (i.e., by modeling the material nonlinearities as a plastic-like constitutive behavior). In addition, a cohesive zone model has been developed (Ref 17) to analyze the effects of the stress-induced martensitic transformation on crack growth

This article is an invited paper selected from presentations at Shape Memory and Superelastic Technologies 2010, held May 16-20, 2010, in Pacific Grove, California, and has been expanded from the original presentation.

C. Maletta, University of Calabria—Mechanical Engineering, P. Bucci 44C, 87030 Arcavacata di Rende, CS, Italy; and **M.L. Young**, Institut fur Werkstoffe, Ruhr-Universitat, Bochum, Germany. Contact e-mail: carmine.maletta@unical.it.

resistance in NiTi SMAs, as well as to simulate the effects of the wake of the crack, which is mainly associated with the reverse martensitic transformation occurring during crack propagation (Ref 10).

Due to the limitations of fracture mechanics theories in analyzing the complex mechanisms and crack tip stress distribution in NiTi SMAs, some analytical models have been developed (Ref 18-24), where the main features and constitutive behavior of NiTi SMAs are included, with the aim of creating effective design criteria and life prediction methods for components with cracks. These models, which use modified fracture mechanics concepts for linear elastic and elasto-plastic materials, are able to predict the boundaries of the transformed region as well as the crack tip stress distribution. Specifically, a simple model, based on linear elastic fracture mechanics concepts, has been proposed by Birman (Ref 18) to estimate the boundaries of transformed martensite near the crack tip. Other models (Ref 19, 20), based on the Eshelby inclusion method (Ref 25), allow for prediction of crack tip stress singularities. More recently, novel analytical models, based on the assumptions of small scale yielding and on modified fracture mechanics theories, have been developed to predict the size of the fully transformed martensite (M), austenite (A), and the transformation zone (A $\rightarrow$ M) under mode I (Ref 22) and mode III (Ref 23) loading conditions. Furthermore, new fracture control parameters for NiTi SMAs have been proposed (Ref 24), based on the model developed in Ref 22. Unfortunately, the usefulness and applicability of these latter models (Ref 22, 24) is limited by some basic assumptions, such as plane stress conditions at the crack tip. This condition is not satisfied in standard tests for fracture toughness measurements, where thick specimens must be used to ensure plane strain conditions and to avoid the formation of a wide plastic zone. To overcome the aforementioned limitation, a new analytical model has been developed by modifying the reference model (Ref 22) to predict the crack tip transformation behavior under both plane stress and plane strain conditions. Furthermore, the model predictions of the boundaries of the transformed region at the crack tip have been compared with synchrotron x-ray micro-diffraction observations on miniature compact tension (CT) specimens (Ref 9).

2. Materials and Experiments

As described in detail in Ref. 9-11, 26, all experimental data presented here was taken from a pseudoelastic NiTi SMA with 50.7 at.% Ni, which had been subjected to thermo-mechanical treatments (forming and aging) and a final heat-treatment for 6 min at 773 K resulting in an average austenite grain size of 70 μm with Ni_4Ti_3 precipitates ranging in size from 60 to 130 nm. The DSC curve for the pseudoelastic NiTi SMA has been reported in Gollerthan et al. (Ref 9). The stress-strain curve in Fig. 1 was obtained during monotonic isothermal loading at room temperature (295 K) of a pseudoelastic NiTi SMA tensile specimen, identical to that reported in Gollerthan et al. (Ref 9). Figure 1 also includes the Young's moduli for austenitic and martensitic structures, E_A and E_M, respectively, as well as the transformation stress and strain, σ^{tr} and ε_L. In the proposed model, the transformation strain ε_L is regarded as a material constant, while the transformation stress σ^{tr} is

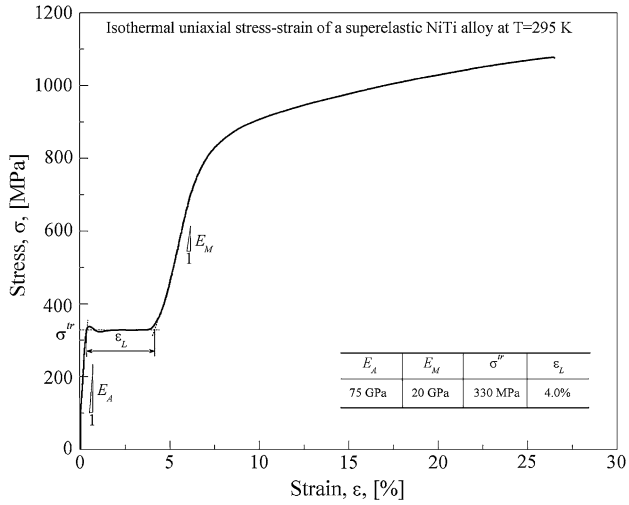

Fig. 1 Monotonic uniaxial stress-strain curve of a pseudoelastic NiTi SMA (50.7 at.% Ni) at room temperature (295 K) (Ref 9)

expressed as a function of the temperature (T) according to the Clausius-Clapeyron relation:

$$\sigma^{tr} = \sigma_0^{tr} + b_M(T - T_0) \qquad \text{(Eq 1)}$$

where σ_0^{tr} is the transformation stress at the reference temperature T_0 and b_M is a material constant.

Here, it should be noted that the Young's modulus E_M illustrated in Fig. 1 does not represent the true Young's modulus of martensite, which is much higher than that of austenite (Ref 27-29). In fact, in addition to the elasto-plastic strain of the martensite, this slope E_M is actually a combination of a small amount of strain which accumulates during the phase transformation, plastic deformation (austenitic), grain reorientation, and detwinning or reorientation of martensite variants (Ref 29-31). However, the proposed model is based on the macroscopic stress-strain response of the material, which is described by the more easily measurable uniaxial stress-strain curve, and the slope of the curve for the fully transformed martensitic structure is used for the effective Young's modulus of martensite.

3. Crack Tip Stress Distribution in SMAs: Basic Assumptions

As schematically illustrated in Fig. 2, the stress-induced martensitic transformation, occurring near the crack tip of NiTi SMAs due to the high local stress values, results in a complex stress distribution with respect to linear elastic materials. In particular, when the equivalent stress (σ_e) exceeds the transformation stress σ^{tr}, three different regions are observed near the crack tip:

(1) Austenitic or untransformed region for $r > r_A$ (i.e., for $\sigma_e < \sigma^{tr}$).
(2) Transformation zone for $r_M \le r \le r_A$ (i.e., for $\sigma_e = \sigma^{tr}$).
(3) Martensitic or fully transformed region for $r < r_M$ (i.e., for $\sigma_e > \sigma^{tr}$)

where r_M and r_A are the radii of the martensitic and austenitic regions, respectively, and define the boundaries of the transformation region for $\theta = 0$ (see Fig. 2).

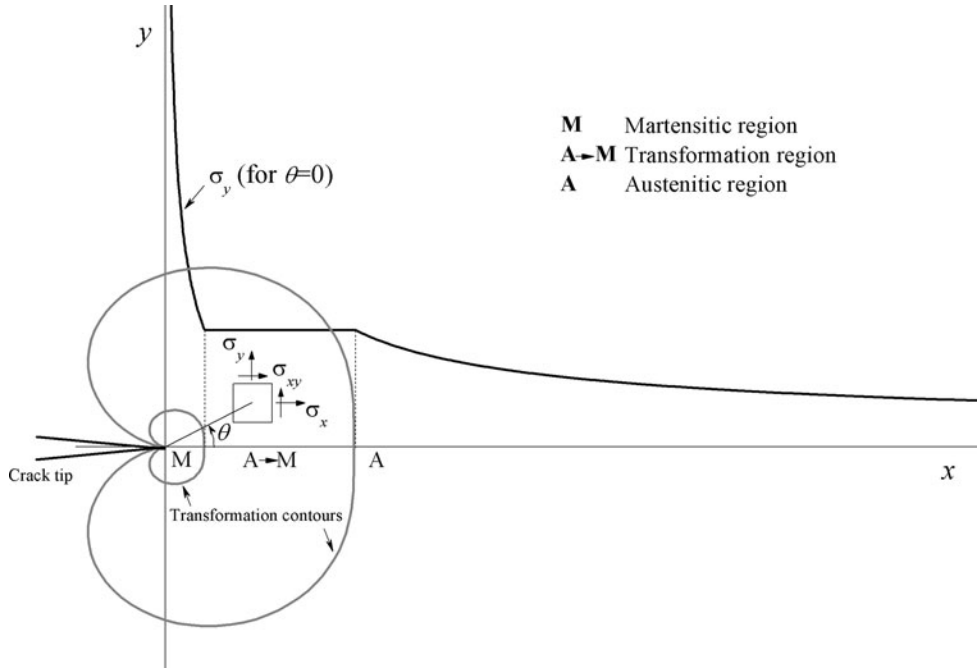

Fig. 2 Schematic depiction of the stress distribution and phase transformation near the crack tip

Due to the complex crack tip stress distribution in SMAs, well-known theories for linear elastic and elasto-plastic materials do not accurately capture the mechanical behavior. Therefore, specific models must be developed, which consider the unique constitutive behavior of SMAs. For this purpose, an analytical model for fracture mechanics of SMAs has been developed and presented here based on a reference model (Ref 22). With respect to this latter model, the present model allows for prediction of the stress distribution as well as the boundaries of the transformation region near the crack tip under both plane stress and plane strain conditions.

In any case, it is important to point out that the following limitations are still present in the proposed model: (i) plastic deformation of martensite is neglected, (ii) the stress-strain hysteretic behavior of the material is not taken into account, and (iii) a flat stress plateau is considered during phase transformation.

The first assumption has a limited impact since plastic deformation is expected to be less important on the fracture behavior of NiTi SMAs than the crack tip transformation mechanisms. In fact, in pseudoelastic NiTi SMAs, it has been shown that cracks propagate in a detwinned martensitic variant microstructure, which is only present after the austenite has been fully transformed to martensite (Ref 9). Therefore, the plastic zone has been shown to be much smaller than the transformation zone and it has been demonstrated that crack tip blunting, which is associated with dislocation plasticity, does not occur in pseudoelastic NiTi SMAs (Ref 9).

The second assumption does not represent a limitation in the case of static or monotonic loading conditions. In this case, the model could be used to develop proper design criteria for critical crack growth since fracture toughness is normally measured by monotonic loading to fracture; however, the applicability of the model for fatigue crack propagation needs to be verified since the reversibility of phase transformation during crack growth is expected to play a significant role, as shown in Ref 10, 17.

Finally, the third assumption does not represent a significant limitation when dealing with commercial pseudoelastic NiTi SMAs, which usually exhibit a completely flat stress-strain transformation curve, similar to that shown in Fig. 1; it can, however, be a major concern when NiTi SMAs are subjected to severe cold-working deformation processes and/or repeated mechanical loads. In fact, due to some irreversible microstructural changes occurring during such processes, mainly attributed to the formation of dislocations and stabilized martensite, the stress-strain response of the SMA changes significantly, i.e., the slope of the stress-strain transformation curve increases and, consequently, the stress for the onset of stress-induced transformation decreases.

Furthermore, it should be mentioned here that the pseudoelastic effect can be significantly improved by plastic deformation (due to the resulting smaller grain size, which limits the mobility of dislocations), while this is commercially easier to perform for applications such as wires (i.e., cold-drawing), it can be more difficult to perform on other applications such as large bulk castings. An alternative approach to improve the pseudoelastic effect is to form Ni_4Ti_3 precipitates, which also limit the mobility of dislocations. It is expected that these two processing methods would exhibit similar mechanical behavior. Nevertheless, one should note that our model is being compared with a pseudoelastic NiTi SMA with Ni_4Ti_3 precipitates.

4. Analytical Model

Some basic concepts of linear elastic fracture mechanics along with a summarization of the reference model (Ref 22) are presented and discussed in this section.

Based on linear elastic fracture mechanics, the crack tip stress components σ_{ij} under mode I loading, as a function of the polar coordinates r and θ, can be written as follows (Ref 32):

$$\sigma_{ij}(r,\theta) = \frac{K_I}{\sqrt{2\pi r}} f_{ij}(\theta), \quad \text{(Eq 2)}$$

where K_I is the mode I stress intensity factor and $f_{ij}(\theta)$ are well-known trigonometric functions of the angle θ. K_I can be expressed as a function of the crack length and applied stress, a and σ^{∞} respectively, as follows:

$$K_I = \beta\sigma^{\infty}\sqrt{\pi a}, \quad \text{(Eq 3)}$$

where β is a geometric factor. In the case of an infinite plate with a through thickness central crack of length $2a$, the factor β is equal to 1 and K_I can be regarded as the applied or remote stress intensity factor, K_I^{∞}, because it is independent of the geometric configuration of the cracked structure:

$$K_I^{\infty} = \sigma^{\infty}\sqrt{\pi a}. \quad \text{(Eq 4)}$$

The applied stress intensity factor is used in the following for comparative analysis between linear elastic materials and NiTi SMAs. If the principal stress directions (identified by the subscripts 1, 2, and 3) are considered, the functions $f_{ij}(\theta)$ in Eq 2 can written as follows (Ref 32):

$$f_1(\theta) = \cos\frac{\theta}{2}\left(1 + \sin\frac{\theta}{2}\right), \quad \text{(Eq 5a)}$$

$$f_2(\theta) = \cos\frac{\theta}{2}\left(1 - \sin\frac{\theta}{2}\right), \quad \text{(Eq 5b)}$$

$$f_3(\theta) = b, \quad \text{(Eq 5c)}$$

where $b = 0$ for plane stress, $b = 2\nu\cos(\theta/2)$ under plane strain conditions and ν is the Poisson's ratio of the material. Note that subscripts 1 and 2 identify the in-plane principal stress directions, while 3 is the direction perpendicular to the plate. In the case of $\theta = 0$ (i.e., along the crack direction), Eq 5a-5c can be simplified and, consequently, the principal stress components for a linear elastic material are given by:

$$\sigma_{el1}(r) = \sigma_{el2}(r) = \frac{K_I}{\sqrt{2\pi r}}, \quad \text{(Eq 6a)}$$

$$\sigma_{el3}(r) = b\frac{K_I}{\sqrt{2\pi r}}. \quad \text{(Eq 6b)}$$

While Eq 6a-6b are generally valid for linear elastic materials, they do not describe the complex crack tip stress distribution in SMAs, where two different stress equations must be used to define the stress distribution in the two phases of the material. It has been observed in Maletta and Furgiuele (Ref 22) that modified relations for elasto-plastic materials, such as the Irwin correction of the stress intensity factor (Ref 33), can be used to predict the stress distribution in the austenitic phase (i.e. in the untransformed region). Specifically, the effective crack length and stress intensity factor (a_e and K_{Ie}, respectively) can be used to take into account the nonlinear effects due to stress-induced phase transformation:

$$a_e = a + \Delta r, \quad \text{(Eq 7)}$$

$$K_{Ie} = \sigma^{\infty}\sqrt{\pi a_e}, \quad \text{(Eq 8)}$$

where the distance Δr is given by Maletta and Furgiuele (Ref 22):

$$\Delta r = r_A - r^*, \quad \text{(Eq 9)}$$

with

$$r^* = \frac{1}{2\pi}\left(\frac{K_I}{f_{tc}\sigma^{tr}}\right)^2, \quad \text{(Eq 10)}$$

where f_{tc} can be regarded as a transformation constraint factor and represents the ratio of the maximum principal stress to the transformation stress σ^{tr} (i.e., the quantity $f_{tc}\sigma^{tr}$ can be considered as an effective transformation stress):

$$f_{tc} = \frac{\sigma_{max}}{\sigma^{tr}}. \quad \text{(Eq 11)}$$

It is worth noting that f_{tc} is calculated based on the plastic constraint factor in linear elastic fracture mechanics (Ref 32) and varies in the range between 1 and $(1-2\nu)^{-1}$ with the lower and upper bounds corresponding to plane stress and plane strain conditions, respectively. However, Irwin (Ref 32) suggested a maximum value of $\sqrt{2\sqrt{2}}$ in the case of elasto-plastic materials, as plane strain conditions do not exist at the specimen surface and, furthermore, crack blunting significantly reduces the maximum stress at the crack tip. Due to the different mechanisms involved during crack loading and propagation in SMAs with respect to common metals, the maximum value of f_{tc} could be different with respect to the plastic constraint factor. In fact, Gollerthan et al. (Ref 9) demonstrated that crack tips stay sharp and blunting does not occurs in either martensitic or pseudoelastic SMAs, which indicates that dislocations at the crack tip do not play a critical role.

Based on the Irwin correction (Ref 33) and on the reference model (Ref 22), the principal stress components in the austenitic region for $\theta = 0$ can be expressed as follows:

$$\sigma_{A1}(r) = \sigma_{A2}(r) = \frac{K_{Ie}}{\sqrt{2\pi(r-\Delta r)}} \quad \text{(Eq 12a)}$$

$$\sigma_{A3}(r) = b\frac{K_{Ie}}{\sqrt{2\pi(r-\Delta r)}} \quad \text{(Eq 12b)}$$

The stress distribution in the martensitic region can be determined by modified relations for bilinear materials according to Duva (Ref 34). Thus, the strain components in the austenitic region (i.e., for $\sigma_e < \sigma^{tr}$) and in the martensitic region (i.e., for $\sigma_e > \sigma^{tr}$) are given by:

$$\varepsilon_{ij} = \frac{1}{E_A}\left[(1+\nu)\sigma_{ij} - \nu\delta_{ij}\sigma_{kk}\right], \quad \text{for } \sigma_e < \sigma^{tr} \quad \text{(Eq 13a)}$$

$$\varepsilon_{ij} = \frac{1}{E_A}\left[(1+\nu)\sigma_{ij} - \nu\delta_{ij}\sigma_{kk} + \frac{3}{2}\left(\alpha^{-1}-1\right)\frac{\sigma_e - \sigma^{tr}}{\sigma_e}S_{ij}\right] + \varepsilon_{ij}^{tr}, \quad \text{for } \sigma_e > \sigma^{tr} \quad \text{(Eq 13b)}$$

where α represents the Young's modulus ratio ($\alpha = E_M/E_A$), δ_{ij} is the Kronecker delta and ε_{ij}^{tr} are the components of the transformation strain tensor. The deviatoric stress components and effective stress, S_{ij} and σ_e, respectively, are defined by:

$$S_{ij} = \sigma_{ij} - \frac{1}{3}\sigma_{kk}\delta_{ij} \quad \text{(Eq 14)}$$

$$\sigma_e = \sqrt{\frac{3}{2}S_{ij}S_{ij}} \quad \text{(Eq 15)}$$

The transformation strain tensor is calculated from the uniaxial transformation strain ε_L by the equivalent von Mises strain ε_e:

$$\varepsilon_e = \sqrt{\frac{2}{3}e_{ij}e_{ij}} \quad \text{(Eq 16)}$$

where e_{ij} represent the deviatoric strain components:

$$e_{ij} = \varepsilon_{ij} - \frac{1}{3}\varepsilon_{kk}\delta_{ij} \quad \text{(Eq 17)}$$

in the case of $\theta = 0$, the strain components ε_{ij}^{tr} can be regarded as principal strains, namely ε_1^{tr}, ε_2^{tr}, and ε_3^{tr}, and are obtained from Eq 16 by imposing the condition $\varepsilon_e = \varepsilon_L$:

$$\begin{aligned}\varepsilon_1^{tr} &= \varepsilon_2^{tr} = \chi\varepsilon_L \\ \varepsilon_3^{tr} &= \xi\varepsilon_L\end{aligned} \quad \text{(Eq 18)}$$

in which $\chi = 1/2$ and $\xi = -1$ under plane stress, and $\chi = 3/2$ and $\xi = 0$ under plane strain conditions. Considering Eq 14-18, Eq 13 can be rewritten in terms of principal strain components as follows:

$$\varepsilon_1 = \frac{\sigma_{A1}}{E_A}\kappa \quad \text{(Eq 19a)}$$

$$\varepsilon_1 = \frac{1}{E_A}\left[\sigma_{M1}\kappa + \frac{1}{2}\left(\alpha^{-1} - 1\right)\left(f_{tc}^{-1}\sigma_{M1} - \sigma^{tr}\right)\right] + \chi\varepsilon_L \quad \text{(Eq 19b)}$$

where κ is given by $\kappa = (1 - \nu)$ for plane stress conditions and $\kappa = (1 + \nu)(1 - 2\nu)$ for plane strain conditions. Comparing Eq 19a-19b and considering Eq 12a gives the principal stress components in the martensitic region:

$$\begin{aligned}\sigma_{M1}(r) = \sigma_{M2}(r) &= \frac{1}{2\kappa + f_{tc}^{-1}(\alpha^{-1} - 1)} \\ &\times \left[2\kappa\frac{K_{Ie}}{\sqrt{2\pi r}} + \left(\alpha^{-1} - 1\right)\sigma^{tr} - 2\chi\varepsilon_L E_A\right]\end{aligned} \quad \text{(Eq 20a)}$$

$$\sigma_{M3}(r) = b\sigma_{M1}(r) \quad \text{(Eq 20b)}$$

The martensitic radius r_M, can be calculated by using the condition $\sigma_{M1}(r_M) = f_{tc}\sigma^{tr}$:

$$r_M = \frac{1}{2\pi}\left[\frac{\kappa K_{Ie}}{f_{tc}\kappa\sigma^{tr} + \chi\varepsilon_L E_A}\right]^2 \quad \text{(Eq 21)}$$

The austenitic radius r_A can be calculated by imposing the equilibrium condition at the crack tip, as described in Ref 22, and, thus, the following relation can be obtained:

$$r_A = 2r^* - \frac{2}{\pi}\left(\frac{\kappa K_{Ie}}{\sigma^{tr}}\right)^2 \frac{1}{(2f_{tc}\kappa + (\alpha^{-1} - 1))}\frac{1}{2f_{tc}\kappa + 2\chi\varepsilon_L E_A/\sigma^{tr}} \quad \text{(Eq 22)}$$

Equation 21 and 22 can be expressed as a function of the temperature when the Clausius-Clapeyron relation of Eq 1 is considered:

$$r_M = \frac{1}{2\pi}\left[\frac{\kappa K_{Ie}}{f_{tc}\kappa\left(\sigma_0^{tr} + b_M(T - T_0)\right) + \chi\varepsilon_L E_A}\right]^2 \quad \text{(Eq 23)}$$

$$r_A = 2r^* - \frac{2}{\pi}\left(\frac{\kappa K_{Ie}}{\sigma^{tr}}\right)^2 \times \frac{1}{(2f_{tc}\kappa + (\alpha^{-1} - 1))}\frac{\sigma_0^{tr} + b_M(T - T_0)}{2f_{tc}\kappa\left(\sigma_0^{tr} + b_M(T - T_0)\right) + 2\chi\varepsilon_L E_A} \quad \text{(Eq 24)}$$

Note that Eq 23 and 24 give the same results in the case of plane stress conditions as those of the reference model (Ref 22). Furthermore, it is worth noting that an iterative approach is required to calculate the transformation radii, r_M and r_A, similar to the classic Irwin's correction for elasto-plastic materials. In particular, the following steps are carried out:

(1) The first trial values of the transformation radii, namely r_M' and r_A', are calculated using Eq 21 and 22 (or alternatively Eq 23 and 24) and the uncorrected stress intensity factor of Eq 3, namely K_I;
(2) The effective crack length and stress intensity factor, a_e and K_{Ie}, are calculated by Eq 7-9;
(3) Based on the effective stress intensity factor calculated in the previous step, new values of the transformation radii, namely r_M'' and r_A'', are calculated using Eq 21 and 22 (or Eq 23 and 24);
(4) Convergence of the solution is checked by comparing the trial and calculated values of the transformation radii. If the results do not meet the convergence criteria (i.e., the relative errors between trial and calculated values of the transformation radii exceed the maximum allowable error), then new trial values are assigned to r_M and r_A ($r_M' = r_M''$ and $r_A' = r_A''$) and steps from 2 to 4 are repeated until convergence is reached.

5. Results and Discussion

In this section, the proposed model is validated by previous synchrotron x-ray micro-diffraction observations (Ref 9); subsequently, the model is used to analyze the evolution of the crack tip transformation region during mechanical loading of miniature CT specimens (Ref 9) under both plane stress and plane strain conditions (i.e., by varying the transformation constraint factor f_{tc}).

The compact tension (CT) specimens discussed in this article correspond to a miniature version of the ASTM CT specimen standard E399-90 (Ref 35) and have been previously described in detail in Ref 9, 11. These CT specimens have widths of $W = 16$ mm and thicknesses of $B = 8$ mm and were fatigue pre-cracked to yield crack lengths a ranging between 8 mm ($a/W = 0.50$) and 11.8 mm ($a/W = 0.74$) (Ref 9).

Analytical predictions of the transformation region in miniature CT specimens are obtained by using Eq 21 and 22 together with the well-known relation for stress intensity factor (ASTM E 399):

$$K_I = \frac{P}{B\sqrt{W}}f\left(\frac{a}{W}\right), \quad \text{(Eq 25)}$$

where P is the applied load and $f\left(\frac{a}{W}\right)$ is given by:

$$f\left(\frac{a}{W}\right) = \frac{(2 + a/W)\left(0.886 + 4.64(a/W) - 13.32(a/W)^2 + 14.72(a/W)^3 - 5.6(a/W)^4\right)}{(1 - a/W)^{3/2}}. \quad \text{(Eq 26)}$$

The values of the effective stress intensity factor for the CT specimen (K_{Ie}) in Eq 21 and 22, are calculated from Eq 25 and 26, instead of Eq 8, using the effective crack length from Eq 7. It is worth noting that an iterative approach is required to calculate the transformation radii as described in the previous section.

In Fig. 3, the contours of the transformation radii for a miniature CT specimen with a crack length-to-width ratio $a/W = 0.55$ under opening mode conditions with a constant load $P = 2860$ N, are illustrated. Figure 3(a) shows a comparison between the predictions of the proposed analytical model, in terms of the austenitic radius r_A, and the phase volume fractions obtained by synchrotron x-ray micro-diffraction mapping of a miniature CT specimen. The analytical predictions were obtained from Eq 22 and 25-26 using the same geometry and loading conditions of the experiment, with the material properties reported in Fig. 1 ($E_A = 75$ GPa, $E_M = 20$ GPa, $\sigma^{tr} = 330$ MPa, $\varepsilon_L = 0.04$) and by assuming that the Poisson's ratio for the two phases are equal (i.e., $\nu_A = \nu_M = \nu = 0.3$). Due to the spatial resolution of the x-ray micro-diffraction technique, only the models for the external transformation contour, i.e., the austenitic radius, is compared with the experimental data in Fig. 3(a); in fact, the martensitic radius r_M is not compared since just the region with a maximum volume fraction of 30-40% martensite (B19′) was observed by the synchrotron x-ray micro-diffraction. For the sake of completeness, the contours of both r_M and r_A are illustrated in Fig. 3(b) under plane stress and plane strain conditions; in particular, the austenitic radius is shown in the first and second quadrants of the Cartesian system, while the martensitic radius is illustrated in the third and fourth quadrants. Figure 3(a) and (b) clearly illustrates that the martensitic radius is significantly smaller than the austenitic radius, especially if considering plane strain conditions, where r_M for $\theta = 0$ is about 20 μm. Furthermore, it is worth noting that the shapes of the transformed region under plane stress and plane strain conditions were obtained using the well-known trigonometric functions for plastic zone in common metals by the von-Mises yielding criteria (Ref 32). However, the shape of the transformed zone could be significantly different with respect to that of plastic zone, due to the different mechanisms involved during crack loading of SMAs with respect to common metals, as discussed in the previous section. In this study, only the transformation boundaries for $\theta = 0$ are analytically calculated and the shape is presented for a qualitative comparison with x-ray micro-diffraction mapping. In particular, the comparison illustrates that the experimentally observed transformation region is between plane stress (black curve) and plane strain contours (red curve). This result is expected since each x-ray micro-diffraction measurement in Fig. 3(a) represents a volume-averaged value through the specimen thickness (i.e., between plane stress at the specimen surfaces and plane strain in the center) as reported in Gollerthan et al. (Ref 9).

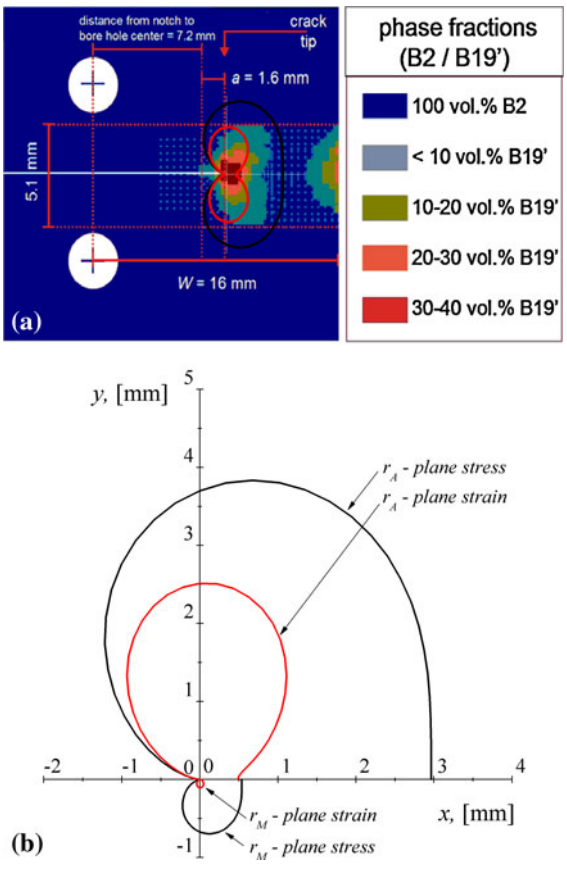

Fig. 3 Contours of the transformation region for a miniature CT specimen with a crack length-to-width ratio $a/W = 0.55$ under a constant load $P = 2860$ N: (a) comparison of the austenitic radius r_A between numerical predictions and experimental observations by synchrotron x-ray micro-diffraction (Ref 9); (b) austenitic radius, r_A, and martensitic radius, r_M, under plane stress and plane strain conditions

In Fig. 4, the evolution of the transformation region during mechanical loading of miniature CT specimens, in terms of r_A and r_M, are illustrated together with the corresponding load-displacement curves (P-δ). In particular, Fig. 4(a) and (b) shows the normalized transformation radii, r_A/a and r_M/a, for two different values of the a/W ratio, equal to 0.5 and 0.6, respectively. The transformation radii as a function of the applied load during tensile testing of miniature CT specimens have been calculated from Eq 21 and 22, using the stress intensity factor from Eq 25. The dashed lines in Fig. 4(a) and (b) indicate the maximum load and, consequently, the maximum size of the transformation region. It should be noted that the evolution of the transformed region, after the maximum load is reached, is not correctly calculated, since the present model does not take into account the hysteretic behavior observed during reverse transformation from austenite to martensite (i.e., only monotonically increasing loads can be analyzed). As expected, Fig. 4(a) and (b) shows large differences in the size of transformed region between plane stress and

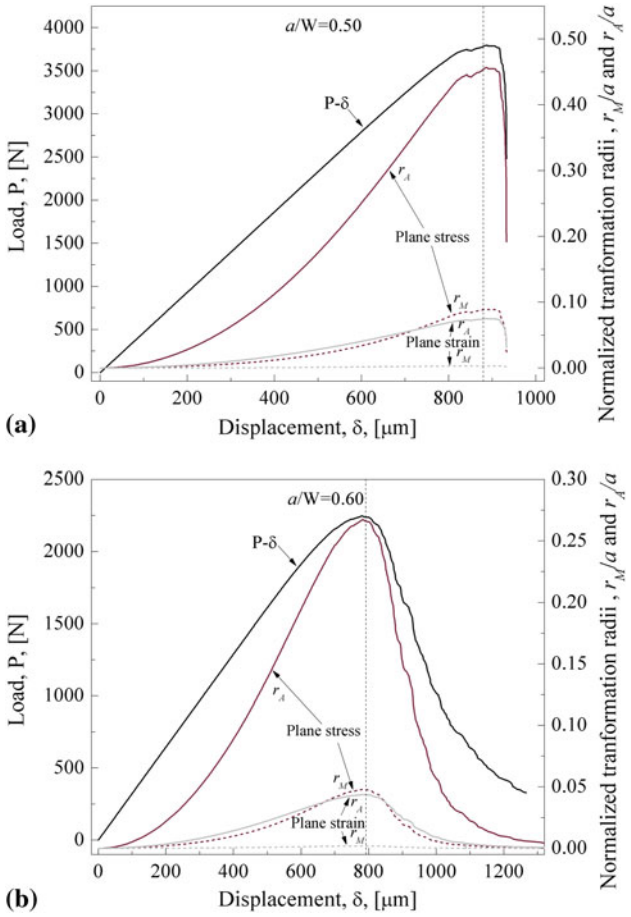

Fig. 4 Evolution of normalized transformation radii, r_A/a and r_M/a, during mechanical loading of two miniature CT specimens with (a) $a/W = 0.5$ and (b) $a/W = 0.6$ (Ref 9)

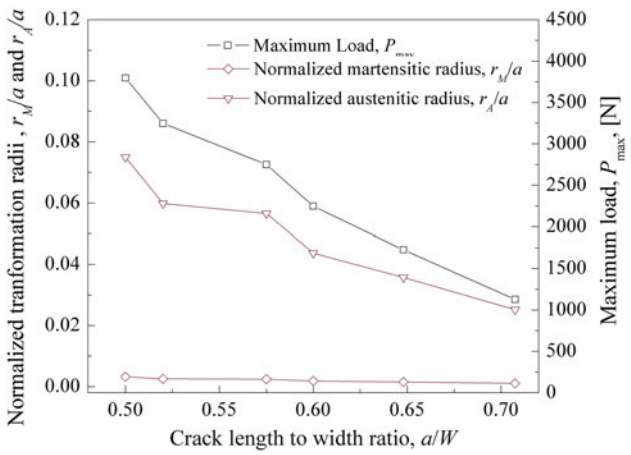

Fig. 5 Maximum load and corresponding normalized transformation radii, r_A/a and r_M/a, for miniature CT specimens with different a/W ratios

plane strain conditions with a ratio close to the theoretical value of $f_{tc}^2 = (1 - 2\nu)^{-2}$ ($f_{tc}^2 = 6.25$ when $\nu = 0.3$), i.e., that of the plastic zone in common engineering metals. Furthermore, Fig. 4(a) and (b) shows that the size of the transformation region in the case of $a/W = 0.5$ (Fig. 4a) is higher than that of the $a/W = 0.6$ (Fig. 4b) as a consequence of the higher values of maximum load.

To better understand the effect of a/W on the boundaries of the transformation region, the data obtained during fracture tests of miniature CT specimens reported in Gollerthan et al. (Ref 9) have been analyzed as illustrated in Fig. 5, which shows the maximum extents of r_A/a and r_M/a as a function of the a/W ratio in the case of plane strain conditions. In the same figure, the maximum load obtained during mechanical testing are also reported.

Figure 5 shows that r_A/a decreases more rapidly with increasing a/W ratio than r_M/a. This result is supported by the fact that the formation of stress-induced martensite is needed for crack growth and propagation. As expected, when the crack length is longer, less load is required for crack propagation due to the smaller cross-sectional area and therefore less stress-induced martensite is required before catastrophic failure occurs.

6. Conclusions

An analytical model which can be used to predict the boundaries of the stress-induced martensitic transformation near a crack tip in pseudoelastic NiTi SMAs, under both plane stress and plane strain conditions, is presented. The predictions of the model show reasonably good agreement with experimental results from synchrotron x-ray micro-diffraction mapping. As expected, the experimental data falls between the plane stress and plane strain contours of the model, due to the fact that the measurements from synchrotron x-ray micro-diffraction represent volume-averaged values through the specimen thickness. Furthermore, the evolution of the transformation region near a crack tip during mechanical loading of miniature compact tension specimens have been analyzed under both plane stress and plane strain conditions.

However, the proposed model uses some simplifying conditions: (i) plastic deformation of martensite is neglected, (ii) the stress-strain hysteretic behavior of the material is not taken into account, and (iii) a flat stress plateau is considered during phase transformation. The results presented here as well as other previous experimental results demonstrate that these latter assumptions do not represent significant limitations on fracture properties of SMAs, as they play a secondary role as compared to stress-induced phase transformation mechanisms. In any case, future studies should be carried out to better understand the role of other microstructural changes near the crack tip, such as grain re-orientation, detwinning, and dislocation plasticity, on fracture properties of NiTi SMAs.

References

1. K. Otsuka and C.M. Wayman, *Shape Memory Materials*, Cambridge University Press, Cambridge, 1998
2. K. Otsuka and X. Ren, Physical Metallurgy of Ti-Ni-Based Shape Memory Alloys, *Prog. Mater. Sci.*, 2005, **50**(5), p 511–678
3. A. Paiva and M.A. Savi, An Overview of Constitutive Models for Shape Memory Alloys, *Math. Probl. Eng.*, 2006, art. no. 56876
4. K. Gall, J. Tyber, G. Wilkesanders, S.W. Robertson, R.O. Ritchie, and H.J. Maier, Effect of Microstructure on the Fatigue of Hot-Rolled and Cold-Drawn NiTi Shape Memory Alloys, *Mater. Sci. Eng. A*, 2008, **486**(1–2), p 389–403

5. S.W. Robertson and R.O. Ritchie, A Fracture-Mechanics-Based Approach to Fracture Control in Biomedical Devices Manufactured from Superelastic Nitinol Tube, *J. Biomed. Mater. Res. B*, 2008, **84**(1), p 26–33
6. S. Daly, A. Miller, G. Ravichandran, and K. Bhattacharya, An Experimental Investigation of Crack Initiation in Thin Sheets of Nitinol, *Acta Mater.*, 2007, **55**, p 6322–6330
7. M.R. Daymond, M.L. Young, J.D. Almer, and D.C. Dunand, Strain and Texture Evolution During Mechanical Loading of a Crack Tip in Martensitic Shape-Memory NiTi, *Acta Mater.*, 2007, **55**, p 3929–3942
8. S.W. Robertson, A. Mehta, A.R. Pelton, and R.O. Ritchie, Evolution of Crack-Tip Transformation Zones in Superelastic Nitinol Subjected to In Situ Fatigue: A Fracture Mechanics and Synchrotron X-ray Microdiffraction Analysis, *Acta Mater.*, 2007, **55**(18), p 6198–6207
9. S. Gollerthan, M.L. Young, A. Baruj, J. Frenzel, W.W. Schmahl, and G. Eggeler, Fracture Mechanics and Microstructure in NiTi Shape Memory Alloys, *Acta Mater.*, 2009, **57**(4), p 1015–1025
10. S. Gollerthan, M.L. Young, K. Neuking, U. Ramamurty, and G. Eggeler, Direct Physical Evidence for the Back-Transformation of Stress-Induced Martensite in the Vicinity of Cracks in Pseudoelastic NiTi Shape Memory Alloys, *Acta Mater.*, 2009, **57**(19), p 5892–5897
11. S. Gollerthan, D. Herberg, A. Baruj, and G. Eggeler, Compact Tension Testing of Martensitic/Pseudoplastic NiTi Shape Memory Alloys, *Mater. Sci. Eng. A*, 2008, **481–482**(1–2), p 156–159
12. C. Maletta, A. Falvo, F. Furgiuele, G. Barbieri, and M. Brandizzi, Fracture Behaviour of Nickel-Titanium Laser Welded Joints, *J. Mater. Eng. Perform.*, 2009, **18**(5–6), p 569–574
13. G.Z. Wang, Effects of Notch Geometry on Stress–Strain Distribution, Martensite Transformation and Fracture Behavior in Shape Memory Alloy NiTi, *Mater. Sci. Eng. A*, 2006, **434**, p 26979
14. X.M. Wang, Y.F. Wang, A. Baruj, G. Eggeler, and Z.F. Yue, On the Formation of Martensite in Front of Cracks in Pseudoelastic Shape Memory Alloys, *Mater. Sci. Eng. A*, 2005, **394**(1–2), p 393–398
15. G.Z. Wang, F.Z. Xuan, S.T. Tu, and Z.D. Wang, Effects of Triaxial Stress on Martensite Transformation, Stress-Strain and Failure Behavior in Front of Crack Tips in Shape Memory Alloy NiTi, *Mater. Sci. Eng. A*, 2010, **527**, p 1529–1536
16. C. Maletta, A. Falvo, F. Furgiuele, and A. Leonardi, Stress-Induced Martensitic Transformation in the Crack Tip Region of a NiTi Alloy, *J. Mater. Eng. Perform.*, 2009, **18**(5–6), p 679–685
17. Y. Freed and L. Banks-Sills, Crack Growth Resistance of Shape Memory Alloys by Means of a Cohesive Zone Model, *J. Mech. Phys. Solids*, 2001, **55**, p 2157–2180
18. V. Birman, On Mode I, Fracture of Shape Memory Alloy Plates, *Smart Mater. Struct.*, 1998, **7**(4), p 433–437
19. S. Yi and S. Gao, Fracture Toughening Mechanism of Shape Memory Alloys Due to Martensite Transformation, *Int. J. Solids Struct.*, 2000, **37**(38), p 5315–5327
20. S. Yi, S. Gao, and L. Shen, Fracture Toughening Mechanism of Shape Memory Alloys Under Mixed-Mode Loading Due to Martensite Transformation, *Int. J. Solids Struct.*, 2001, **38**(24–25), p 4463–4476
21. F. Xiong and Y. Liu, Effect of Stress-Induced Martensitic Transformation on the Crack Tip Stress-Intensity Factor in Ni-Mn-Ga Shape Memory Alloy, *Acta Mater.*, 2007, **55**(16), p 5621–5629
22. C. Maletta and F. Furgiuele, Analytical Modeling of Stress-Induced Martensitic Transformation in the Crack Tip Region of Nickel–Titanium Alloys, *Acta Mater.*, 2010, **58**, p 92–101
23. S. Desindes and S. Daly, The Small-Scale Yielding of Shape Memory Alloys Under Mode III, Fracture, *Int. J. Solids Struct.*, 2010, **47**, p 730–737
24. C. Maletta and F. Furgiuele, Stress Intensity Factor in Shape Memory Alloys, *Proc. of Int. Conf. on Shape Memory and Superelastic Technology 2010*, Pacific Grove, CA, May 16–20, 2010.
25. J.D. Eshelby, The Determination of the Elastic Field of an Ellipsoidal Inclusion, and Related Problems, *Proc. R. Soc. Lond. A*, 1957, **241**, p 376–396
26. L.-G. Bujoreanu, M.L. Young, S. Gollerthan, C. Somsen, and G. Eggeler, Influence of Heat Treatment and Microstructure on the Tensile Pseudoelastic Response of an Ni-Rich NiTi Shape Memory Alloy, *Int. J. Mater. Res.*, 2010, **101**(5), p 623–630
27. S. Rajagopalan, A.L. Little, M.A.M. Bourke, and R. Vaidyanathan, Elastic Modulus of Shape-Memory NiTi from In Situ Neutron Diffraction During Macroscopic Loading, Instrumented Indentation, and Extensometry, *Appl. Phys. Lett.*, 2005, **86**(8), art. no 081901
28. M.F.-X. Wagner and W. Windl, Lattice Stability, Elastic Constants and Macroscopic Moduli of NiTi Martensites from First Principles, *Acta Mater.*, 2008, **56**, p 6232–6245
29. M.L. Young, M.F.-X. Wagner, J. Frenzel, W.W. Schmahl, and G. Eggeler, Phase Volume Fractions and Strain Measurements in an Ultrafine-Grained NiTi Shape-Memory Alloy During Tensile Loading, *Acta Mater.*, 2010, **58**, p 2344–2354
30. Y. Liu and H. Xiang, Apparent Modulus of Elasticity of Near-Equiatomic NiTi, *J. Alloys Compd.*, 1998, **270**, p 154–159
31. R. Heinen, K. Hackl, W. Windl, and M.F.-X. Wagner, Microstructural Evolution During Multiaxial Deformation of Pseudoelastic NiTi Studied by First-Principles-Based Micromechanical Modeling, *Acta Mater.*, 2009, **57**, p 3856–3867
32. D. Broek, *Elementary Engineering Fracture Mechanics*, 4th ed., Kluwer Academic Publisher, Dordrecht, 1986
33. G.R. Irwin, Plastic Zone Near A Crack and Fracture Toughness, *Proceedings of Seventh Sagamore Ordnance Materials Conference*, Syracuse University Press, Syracuse, NY, 1960, p 63–78
34. J.M. Duva, Singularity at the Apex of a Rigid Wedge Embedded in a Nonlinear Material, *J. Appl. Mech. Trans. ASME*, 1988, **55**(2), p 361–364
35. American Society for Testing and Materials, Designation E399-90, *Annual Book of ASTM Standards*, 1991, p 408